Atmos. Chem. Phys., 25, 8147–8161, 2025
https://doi.org/10.5194/acp-25-8147-2025

Atmospheric Chemistry and Physics
Open Access
EGU

Observation and modeling of atmospheric OH and HO_2^* radicals at a subtropical rural site and implications for secondary pollutants

Zhouxing Zou[1,★], Tianshu Chen[1,★], Qianjie Chen[1], Weihang Sun[1], Shichun Han[1], Zhuoyue Ren[2], Xinyi Li[2], Wei Song[2], Aoqi Ge[2], Qi Wang[2], Xiao Tian[2], Chenglei Pei[3], Xinming Wang[2], Yanli Zhang[2], and Tao Wang[1]

[1]Department of Civil and Environmental Engineering, The Hong Kong Polytechnic University, Hong Kong SAR 999077, China
[2]Guangzhou Institute of Geochemistry, Chinese Academy of Sciences, Guangzhou 510640, China
[3]Guangdong Province Guangzhou Ecological Environment Monitoring Center Station, Guangzhou 510030, China
★These authors contributed equally to this work.

Correspondence: Tao Wang (tao.wang@polyu.edu.hk)

Received: 15 October 2024 – Discussion started: 18 October 2024
Revised: 3 May 2025 – Accepted: 5 May 2025 – Published: 30 July 2025

Abstract. HO_x radicals (OH and HO_2) are crucial oxidants that determine atmospheric oxidation capacity and the production of secondary pollutants; however, their sources and sinks remain incompletely understood in certain rural, forest, and maritime environments. This study measured HO_2^* (HO_2 + contribution from RO_2, organic peroxyl radicals) and OH concentrations using a chemical ionization mass spectrometer at a subtropical rural site in southern China from 12 November to 19 December 2022. The average peak concentrations were $3.50 \pm 2.47 \times 10^6$ cm^{-3} for OH and $1.34 \pm 0.93 \times 10^8$ cm^{-3} for HO_2^*. Model-estimated contribution from RO_2 to HO_2 during the measurement period ranged from 44 % to 69 % of HO_2^*. Calculations based on an observation-constrained chemical model revealed an overestimation of HO_2 and OH concentrations during warm periods of the field study. Sensitivity tests suggest that adding HO_x sinks or an HO_2 recycle process to the model could improve the model performance. Over-simulation of HO_x in the model resulted in overestimations of midday (10:00–15:00 UTC) production rates by more than 79 % for ozone and a factor of 1.88 for nitric acid. Our study highlights the need for further improving understanding of the sources and sinks of OH and HO_2 and representation of them in air quality models.

1 Introduction

The HO_x family, comprising hydroxyl (OH) and peroxy radicals (HO_2), plays a pivotal role in the Earth's atmosphere by driving photochemical processes that influence the air composition and chemistry. OH radicals are primarily produced by the photolysis of ozone (O_3), nitrous acid (HONO), and ozonolysis of alkenes. They initiate the oxidation of CO and most volatile organic compounds (VOCs), producing HO_2 and other organic peroxyl radicals (RO_2, where R represents an organic group such as alkyl, acyl, or aryl). HO_2 is also generated from the photolysis of oxygenated VOCs (OVOCs) and by reactions between OVOCs and OH. In the presence of NO, RO_2 radicals are converted to HO_2 and then to OH radicals, buffering OH concentrations and maintaining atmospheric oxidation capacity (Stone et al., 2012). These interactions are crucial in the formation of photochemical smog and secondary organic aerosol (SOA), which generate NO_2, O_3, and highly oxygenated molecules. HO_x ($OH + HO_2$) radicals are removed through reactions of OH

with inorganic trace gases, self-reactions among radicals, peroxyacetyl nitrate (PAN) formation, and the heterogeneous uptake by aerosols. These processes subsequently contribute to atmospheric acidification and aerosol formation through the production of H_2SO_4 and HNO_3. See Fig. S1 and Table S1 in the Supplement for detailed processes and chemical reactions.

The accuracy of model-predicted OH is a crucial indicator for assessing our understanding of atmospheric processes (Heard and Pilling, 2003). There is a long-standing debate regarding the discrepancies between simulated and observed radical concentrations under low-NO_x conditions, which remains a significant issue (Hofzumahaus et al., 2009; Stone et al., 2012; Zou et al., 2023). Previous studies have shown that models generally predict OH levels well in polluted conditions (NO $>$ 1 ppb), but notable overestimations were observed under low-NO and aged conditions, such as in coastal areas (Kanaya et al., 2007; Zou et al., 2023), marine boundary layers (Berresheim et al., 2002; Carslaw et al., 1999), and rural areas (Bottorff et al., 2023; Kanaya et al., 2012). Missing OH sinks from both measurements and chemical mechanisms were proposed as the primary reason for the overestimation (Lou et al., 2010; Yang et al., 2016; Hansen et al., 2014; Thames et al., 2020). Underestimations of OH concentrations were also observed in high-biogenic-VOC (BVOC) and low-NO ($<$ 1 ppb) conditions, which generally happen in subtropical or tropical areas (Hofzumahaus et al., 2009; Lelieveld et al., 2008; Tan et al., 2001; Whalley et al., 2011). After considering a new OH regeneration mechanism (Wennberg et al., 2018; Novelli et al., 2020) and measurement interference (Feiner et al., 2016; Hens et al., 2014; Mao et al., 2012; Novelli et al., 2014; Woodward-Massey et al., 2020), daytime OH concentrations could be reasonably reproduced by the model in high-BVOC conditions, with some unresolved underestimation in the evening (Jeong et al., 2022; Lew et al., 2020; Tan et al., 2019). Those results call for more measurement and modeling in subtropical and tropical rural areas.

HO_2 concentrations were consistently underpredicted in polluted urban sites (Ma et al., 2019, 2022; Yang et al., 2021), with no clear trends in relatively clean regions. Some studies reported good agreement between measurement and model prediction (Feiner et al., 2016; Lew et al., 2020), whereas others indicated model overprediction (Bottorff et al., 2023; Griffith et al., 2013) and underprediction (Whalley et al., 2010; Kim et al., 2013; Mallik et al., 2018; Tan et al., 2017). These discrepancies may be attributed to several factors, including measurement interference caused by RO_2 recycling in environments rich in BVOCs or aromatics (Fuchs et al., 2011), uncertainties associated with heterogeneous uptake in box models (Yang et al., 2022), and the outflow (or entrainment) of reservoir species like PAN (Griffith et al., 2013; Whalley et al., 2010). Despite these advances, it remains difficult to pin down the exact causes of the model–measurement discrepancies in some of the previous studies.

In the present study, we measured concentrations of OH and HO_2^* (HO_2 + contribution from RO_2) using a quadrupole chemical ionization mass spectrometer (PolyU-CIMS) from November to December 2022 at a subtropical rural site in southern China. We tested the model's capability in reproducing the radical concentrations and elucidating factors contributing to discrepancy under varying temperatures, VOCs, and NO_x conditions. The Methodology section describes the measurement site, the principles and the configuration of PolyU-CIMS, and the setup of chemical box models. The "Results and discussion" section details our findings, providing an analysis of the radical concentrations and exploring the discrepancies between observed data and model predictions. By employing an observation-constrained box model, we analyzed the radical budgets and investigated potential causes for these discrepancies. The study concludes with a discussion of the implications of these findings.

2 Methodology

2.1 Measurement site

The field campaign was conducted at the Conghua Liangkou Air Monitoring Station (23°44′47″ N, 113°47′06″ E; 200 m above sea level) from 12 November to 19 December 2022 (Fig. 1). The site is located at the northern part of the Pearl River Delta (PRD), approximately 80 km from densely populated areas. It is nestled within the Liuxi River National Forest Park (an evergreen broadleaf forest). The site is situated just north of the G105 national highway and around 0.5 km east of Liangkou. Even though it is close to the road, traffic was generally limited during the observation period due to the coronavirus disease (COVID-19) pandemic. The site is subject to BVOC emissions, predominantly isoprene, from the surrounding forest when the daytime temperatures exceeds 20 °C and NO emissions from the nearby national highway, particularly during periods of low wind speeds. The measurements included trace gases such as O_3, NO, NO_2, CO, HONO, VOCs, and OVOCs and meteorological data such as relative humidity (RH), temperature, and photolysis frequencies of HONO, NO_2, O_3, H_2O_2, and HCHO. Details about the instruments are shown in Table S2.

2.2 Radical measurement principle

OH and HO_2^* radicals were measured using the Hong Kong Polytechnic University's quadrupole chemical ionization mass spectrometer (PolyU-CIMS), which had been used in a previous study for OH measurement (Zou et al., 2023). The use of CIMS for OH measurement was pioneered by Eisele and Tanner (1991), with subsequent enhancements in measurement accuracy (Eisele and Tanner, 1993; Tanner et al., 1997; Tanner and Eisele, 1995) and the adoption of inlets for simultaneous measurements of HO_2 and RO_2 (Ed-

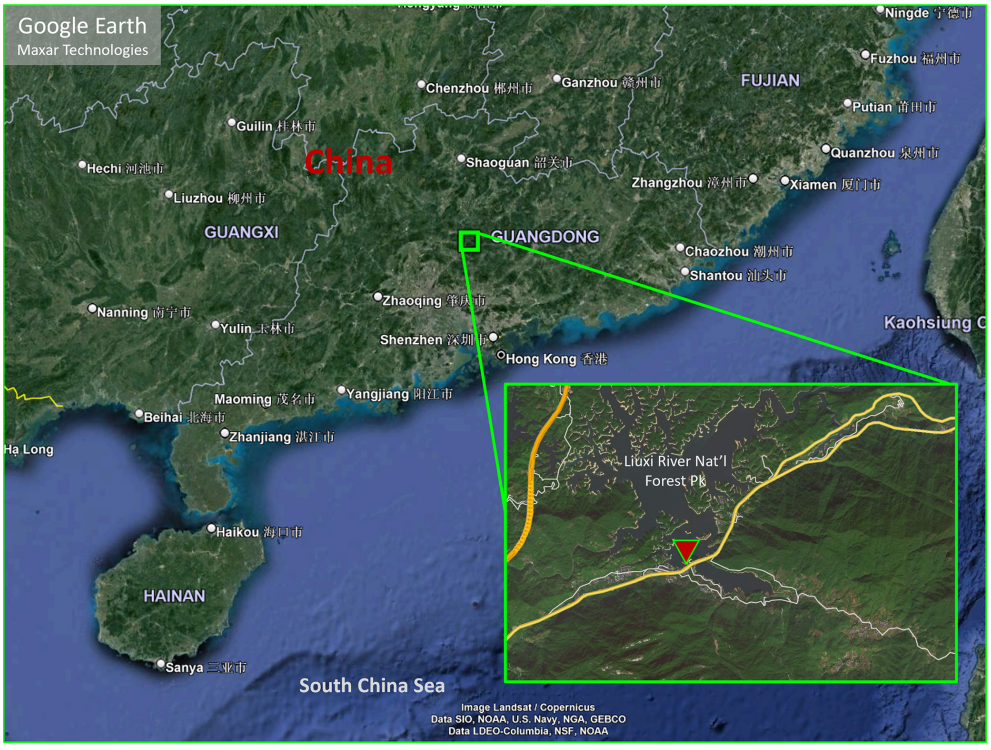

Figure 1. Geographic location of the measurement site (Liangkou Air Monitoring Station; 23°44′47″ N, 113°47′06″ E; 200 m a.s.l.; marked by the inverted red triangle) in Conghua, Guangdong Province, southern China. The map is sourced from © Google Earth and © Amap.

wards et al., 2003; Sjostedt et al., 2007), H_2SO_4 (Mauldin et al., 2004), and OH reactivity (Muller et al., 2018).

Figure 2 illustrates the measurement principle of PolyU-CIMS used in this campaign. Briefly, the ambient OH radicals are converted to H_2SO_4 in the sample inlet system by reacting with SO_2 (Reaction SR21 in Table S1). These are then transformed to HSO_4^- ion clusters in the ionization chamber by the reactions with a reagent gas in sheath flow (HNO_3, Reactions SR24 to SR27 in the Supplement) and are ultimately dissociated (Reaction SR29) for detection by the mass spectrometer system at m/z 97 (S_{97SO_2} in Fig. 2). To mitigate interference and noise, scavenger gases (C_3F_6 in this study) were introduced to scavenge the ambient OH, creating a background signal (Reaction SR23, $S_{97ScaSO_2}$ in Fig. 2). See Text S1 in the Supplement for details about scavenging efficiency. The ambient OH radical signal (S_{OH}) is then determined by subtracting $S_{97ScaSO_2}$ from S_{97SO_2}. The OH concentration is calculated using the following equation:

$$[OH] = \frac{1}{C_{OH}} \times \frac{S_{OH}}{S_{62}}, \quad (1)$$

where C_{OH} represents the calibration factors of OH, and S_{62} is the signal corresponding to the reagent ion (NO_3^-). A detailed calibration procedure for OH is outlined in previous studies (Kürten et al., 2012; Zou et al., 2023) and also in Text S2. Ambient and injected NO can interfere with OH measurements through reaction of $NO + HO_2$. The interference by ambient NO is estimated using a model (within a range of 10^4–10^5 cm^{-3}) and is subtracted from the ambient OH measurements (see Text S3). The interference from the injected NO after HO_2 measurement is discussed in Text S3 and is mitigated through the duty cycle configuration described in Text S4.

To measure ambient HO_2, NO is injected into the sample flow, converting HO_2 to OH (Reaction SR11). This converted OH then follows the same reaction pathway (Reactions SR21, SR24 to SR27, and SR29) and is measured at m/z 97 (S_{97NO} in Fig. 2). Similar to the OH measurement, the background signal for HO_2 ($S_{97ScaNO}$ in Fig. 2) is determined by introducing the scavenger gas. The corresponding signal for ambient HO_2 (S_{HO_2}, as shown in Fig. 2) is determined by subtracting $S_{97ScaNO}$ and S_{OH} from S_{97NO}. The HO_2 concentration is calculated using an equation similar to Eq. (1) by replacing S_{OH} and C_{OH} with S_{HO_2} and C_{HO_2}, respectively (Eq. 2).

$$[HO_2] = \frac{1}{C_{HO_2}} \times \frac{S_{HO_2}}{S_{62}} \quad (2)$$

The procedure for determining the HO_2 calibration factor, C_{HO_2}, is akin to that for C_{OH} (Text S2). The calibration tube generates equal amounts of radicals (Reaction SR30 in the Supplement, $[OH]/[HO_2] = 1$), allowing for simultaneous calibration of HO_2 and OH with and without NO addition to the sample flow.

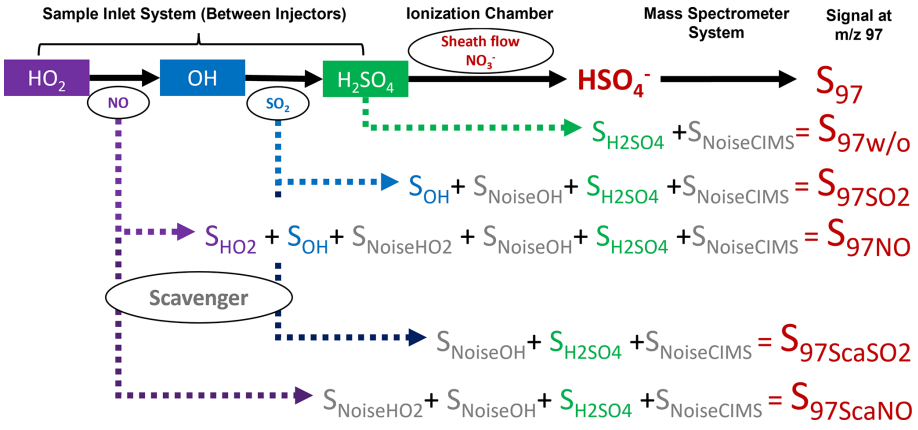

Figure 2. Flowchart depicting the relationship between measurement species and signal intensity at m/z 97 (S_{97}) with various gas injections. The color-filled grids label the ambient species, while the oval shapes label the species injected into the sample flow. Signal intensities with different gas additions to the sample flow are represented by $S_{97\mathrm{w/o}}$, $S_{97\mathrm{SO_2}}$, $S_{97\mathrm{NO}}$, $S_{97\mathrm{ScaSO_2}}$, and $S_{97\mathrm{ScaNO}}$. The signals correspond to ambient OH, HO_2, H_2SO_4, and noise from OH measurement, HO_2 measurement, and the CIMS are denoted as S_{OH}, $S_{\mathrm{HO_2}}$, $S_{\mathrm{H_2SO_4}}$, S_{NoiseOH}, $S_{\mathrm{NoiseHO_2}}$, and $S_{\mathrm{NoiseCIMS}}$, respectively.

In addition to HO_2, the added NO can also react with RO_2 and produce HO_2, which is a potential interference, leading to an overestimation of ambient HO_2 levels (Edwards et al., 2003; Hanke et al., 2002; Fuchs et al., 2011, 2014; Whalley et al., 2013). For our CIMS configuration, the model-estimated daytime interference from RO_2 ranged from 44 % to 69 % of the HO_2^* during the field study (Text S3). Considering the uncertainties in RO_2 mechanisms in the MCM model, we opted not to use model results to correct RO_2 interference, and we denote our HO_2 measurement hereafter as HO_2^*, which is the maximum value of the ambient HO_2 concentrations.

Compared to the configuration of PolyU-CIMS in the previous campaign (Zou et al., 2023), the instrument has been upgraded for simultaneous HO_2^* measurements. Refer to Fig. S2 and Text S5 for the modification to the HO_2^* measurement and to Text S4 for the measurement duty cycle. Apart from these modifications, the settings and configurations of PolyU-CIMS remained the same as those in the previous campaign (see Table S3). With the updated configuration, PolyU-CIMS achieved simultaneous measurement of OH, HO_2^*, and H_2SO_4.

The calibration factors, detection limits, and uncertainties were 1.09×10^{-8}, 3×10^5 cm^{-3}, and 44 % for OH and 1.07×10^{-8}, 2×10^6 cm^{-3}, and 222 % for HO_2^*, respectively (Table S3). The large uncertainty in HO_2^* reflects the possible contribution of RO_2 interference, as discussed previously.

2.3 Box model

HO_x concentrations in this study were simulated using the Framework for 0-D Atmospheric Modelling (F0AM; Wolfe et al., 2016) with the Master Chemical Mechanism (MCM) v3.3.1 (https://mcm.york.ac.uk/MCM/, last access: 24 July 2025), which encompasses over 6700 species and 17 000 reactions. MCM v3.3.1 features a near-explicit chemical mechanism that includes isoprene degradation and OH regeneration mechanisms. This mechanism has previously been employed to investigate HO_x chemistry and conduct budget analyses (Slater et al., 2020; Tan et al., 2018; Zou et al., 2023). The gas-phase chlorine chemistry described by Xu et al. (2015) and Wang et al. (2019) was included in the model (Chen et al., 2022).

In the baseline scenario, the observation data were aggregated into 1 h intervals to provide input for the model, initially constraining it without incorporating observed OH and HO_2^* data. For the assessment of ozone formation rates, the model was adjusted to include constraints based on the actual measured concentrations of OH and HO_2^*. Observed VOCs were categorized into anthropogenic origin (AVOCs), including species from petroleum gas and industrial solvent evaporation (alkanes, alkenes, benzene, and TEX – toluene, ethylbenzene, and xylene), and OVOCs, comprising aldehydes, ketones, and acids. The sole BVOC measured in this study was isoprene. Physical processes like deposition and entrainment in the model were represented by a first-order physical loss with a 24 h lifetime for all species (Chen et al., 2022; Wolfe et al., 2016; Zou et al., 2023). The model also included the heterogeneous uptake of HO_2 by aerosols, represented as a pseudo-first-order loss (Jacob, 2000):

$$\frac{\mathrm{d}[\mathrm{HO_2}]}{\mathrm{d}t} = -k_{\mathrm{HO_2}}[\mathrm{HO_2}], \tag{3}$$

$$k_{\mathrm{HO_2}} = \frac{V_{\mathrm{HO_2}} \times S_{\mathrm{a}} \times \gamma_{\mathrm{HO_2}}}{4}, \tag{4}$$

$$v_{\mathrm{HO_2}} = \sqrt{\frac{8RT}{\pi \times M_{\mathrm{HO_2}}}}. \tag{5}$$

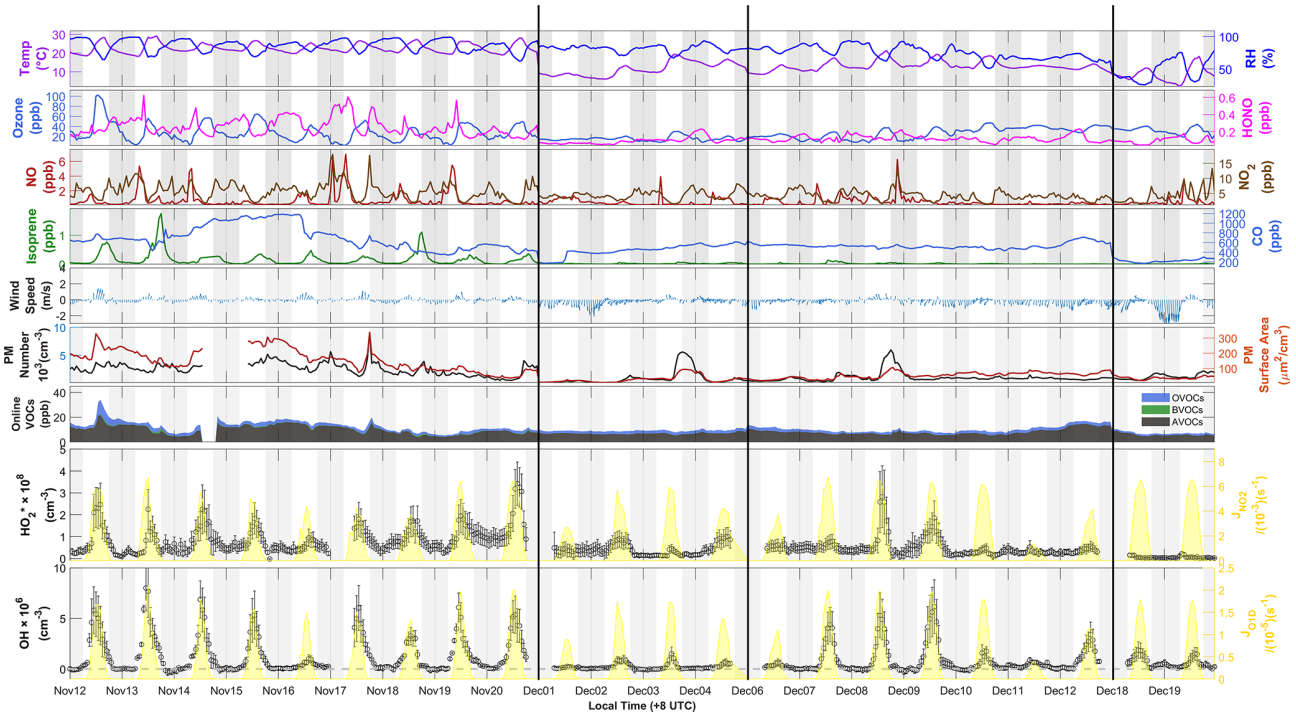

Figure 3. Time series of HO_2^* and OH radicals from 12 November to 19 December 2022, showing measured weather conditions (temperature, RH, wind speed, and wind direction), primary sources of HO_x radicals (ozone, HONO), important sinks of the radicals (CO, isoprene, and VOCs), and photolysis frequencies of NO_2 (J_{NO_2}) and ozone (J_{O1D}). Non-continuous days during the campaign are delineated by the black line. The PRD, CEC, and CNC periods for further analysis are labeled in red, orange, and blue, respectively. The x axis is in local time (+08:00 UTC).

Here, k_{HO_2} represents the first-order loss rate coefficient of HO_2 by aerosol uptake, determined by the effective HO_2 uptake coefficient γ_{HO_2} (0.1, Guo et al., 2019), the mean molecular velocity of HO_2 (v_{HO_2}), the aerosol surface area concentration (S_a) measured by a scanning mobility particle sizer (SMPS), and the molecular mass of HO_2 ($M_{HO_2} = 17\,g\,mol^{-1}$). As aerosol- and aqueous-phase chemistry was not included in the model, it was assumed that the heterogeneous HO_2 loss would not lead to further reactions (Guo et al., 2019). For each day, a 3 d spin-up was performed with constant inputs to establish stable model chemistry and reduce the uncertainty in unconstrained species. Refer to Text S3 for details on the model setup for interference assessment.

3 Results and discussion

3.1 Results from observations

3.1.1 Overview

Figure 3 illustrates a time series showing observed concentrations of radical and trace gases, along with meteorological parameters, from 12 November to 19 December 2022. In November, the conditions were characterized by warm temperatures ranging from 29 to 19 °C and high relative humidity averaging 86 %. In contrast, December witnessed a significant decrease in temperature (ranging from 20 to 9 °C) and a reduction in relative humidity (averaging 72 %). Wind speeds during the campaign were generally low, averaging $0.9 \pm 0.6\,m\,s^{-1}$ and typically remaining below $3.0\,m\,s^{-1}$, with higher speeds occurring towards the end of December. In November, daytime winds predominantly blew from the south, while nighttime winds came from the north. In December, northerly winds predominated both day and night. Detailed hourly wind speed and direction data are illustrated in Fig. 3, and wind roses are shown in Fig. S3. On days with low wind speeds (less than $0.5\,m\,s^{-1}$), NO_x emissions from the G105 national highway significantly influenced chemical measurements at the monitoring site, causing morning NO levels to peak at several parts per billion (ppb). Isoprene concentrations peaked in the afternoons, ranging from 0.2 to 1.7 ppb in November and dropping to less than 0.1 ppb in December. Other trace gases and particulate matter levels were higher in November than in December.

Throughout the campaign, the daytime concentrations of OH and HO_2^* consistently exceeded detection limits and showed distinct diurnal patterns. OH concentrations typically peaked around midday (10:00–15:00 UTC, referred to hereafter in this paper), while HO_2^* levels reached their maximum approximately 1 to 2 h later (Fig. S4). The daily

Table 1. Average values and standard deviations of measured species and parameters throughout the entire campaign (Total) and the selected 3 d cases from each cluster (PRD, CEC and CNC).

Species (unit)	Total	PRD	CEC	CNC
AveMax OH_{Obs} 10^6 (cm^{-3})	3.5 ± 2.5	6.9 ± 1.1	4.9 ± 1.5	5.3 ± 0.9
OH_{Obs} 10^6 (cm^{-3})	0.9 ± 1.5	1.6 ± 2.2	1.4 ± 1.6	1.2 ± 1.8
OH_{DL} 10^6 (cm^{-3})	0.5 ± 0.3	0.4 ± 0.3	0.4 ± 0.2	0.9 ± 0.6
AveMax HO_2 $_{Obs}$ 10^8 (cm^{-3})	1.34 ± 0.93	2.32 ± 1.25	2.36 ± 0.92	1.82 ± 1.02
$HO_{2*_{Obs}}$ 10^8 (cm^{-3})	0.59 ± 0.51	0.76 ± 0.63	1.10 ± 0.68	0.67 ± 0.55
$HO_{2*_{DL}}$ 10^8 (cm^{-3})	0.19 ± 0.11	0.17 ± 0.10	0.25 ± 0.08	0.26 ± 0.15
Pressure (hPa)	995 ± 4	992 ± 1	992 ± 1	995 ± 2
Temp (°C)	16 ± 6.1	23 ± 3.0	23 ± 2.6	14 ± 2.8
RH (%)	78 ± 15	87 ± 11	86 ± 10	81 ± 9.4
Wind Speed ($m\,s^{-1}$)	0.91 ± 0.65	0.53 ± 0.32	0.57 ± 0.34	0.87 ± 0.5
J_{O1D} 10^{-6} (s^{-1})	3.2 ± 5.4	3.5 ± 6	3.6 ± 5.9	4.0 ± 6.6
J_{NO_2} 10^{-3} (s^{-1})	1.3 ± 1.9	1.3 ± 2.1	1.4 ± 2	1.6 ± 2.3
HONO (ppb)	0.169 ± 0.104	0.249 ± 0.084	0.201 ± 0.070	0.133 ± 0.033
SO_2 (ppb)	0.5 ± 0.8	0.5 ± 0.6	0.4 ± 0.5	0.4 ± 0.5
NO_2 (ppb)	4.89 ± 2.37	6.25 ± 2.47	4.84 ± 2.23	4.52 ± 1.97
NO (ppb)	0.57 ± 0.86	0.73 ± 1.09	0.69 ± 1.00	0.73 ± 0.85
CO (ppb)	557.36 ± 225.92	739.41 ± 153.84	464.73 ± 74.34	513.36 ± 22.02
Ozone (ppb)	25 ± 14	32 ± 23	24 ± 13	19 ± 9.4
Particle surface area ($\mu m^2\,cm^{-3}$)	86 ± 72	186 ± 51	84 ± 28	48 ± 19
Isoprene (ppb)	0.082 ± 0.174	0.257 ± 0.337	0.155 ± 0.200	0.029 ± 0.030
OVOCs (ppb)	2.218 ± 1.056	3.163 ± 2.324	1.755 ± 0.379	1.730 ± 0.330
AVOCs (ppb)	8.346 ± 3.223	9.662 ± 5.031	6.886 ± 1.755	6.801 ± 0.864
TEXS (ppb)	0.356 ± 0.316	0.801 ± 0.616	0.266 ± 0.090	0.237 ± 0.085

Note: OVOCs – oxygenated VOCs; AVOCs – anthropogenic VOCs; TEXS – toluene, ethylbenzene, xylene, and styrene. For the average mixing ratio of each measured VOC, refer to Table S4.

maximum concentration of OH varied significantly, ranging from $8.00 \times 10^6\,cm^{-3}$ to nearly the detection limit of $2.54 \times 10^5\,cm^{-3}$, with an average of $3.50 \pm 2.47 \times 10^6\,cm^{-3}$ (Table 1). Similarly, the daily maximum concentration of HO_2^* varied from 3.42×10^8 to $2.17 \times 10^7\,cm^{-3}$, averaging $1.34 \pm 0.93 \times 10^8\,cm^{-3}$ (Table 1). At nighttime, while HO_2^* levels generally remained above the detection threshold, OH concentrations frequently approached the threshold. The average nighttime concentrations were $3.92 \times 10^7\,cm^{-3}$ for HO_2^* and $1.64 \times 10^5\,cm^{-3}$ for OH. We compared the observed OH and HO_2^* concentrations with those reported in previous studies conducted in urban, suburban, rural forest, and coastal sites. As illustrated in Fig. S5, OH concentrations were generally lower than those found in urban settings but similar to levels observed in suburban, rural, and forest environments. This suggests a moderate level of anthropogenic activity typical of mixed rural settings. In contrast, HO_2^* concentrations during these periods were significantly lower than earlier observations in rural and forest environments, likely owing to reduced photochemical activity during our measurement period.

Figure 4 illustrates the results of the 24 h backward-trajectory analysis, revealing three distinct but sequentially occurring phases. In the initial phase (Fig. 4a), air masses originated from the urban and industrial zones of the Pearl River Delta (PRD). This phase was characterized by intense photochemical activity, with ambient temperatures exceeding 20 °C and relative humidity levels surpassing 70 %. During this period, notably high concentrations of VOCs, ozone, and radicals were observed, with the average daily maximum concentrations of OH and HO_2^* radicals reaching $6.50 \pm 1.19 \times 10^6$ and $2.20 \pm 0.27 \times 10^8\,cm^{-3}$, respectively. The subsequent phase was characterized by air masses originating from central eastern China (CEC; Fig. 4b). This phase showed reduced photochemical reactivity and lower concentrations of the measured trace gases. The average daily maximum concentrations of OH and HO_2^* during this phase were $4.35 \pm 2.19 \times 10^6$ and $1.96 \pm 0.90 \times 10^8\,cm^{-3}$, respectively. The final phase was influenced by air masses from central northern China (CNC; Fig. 4c), which exhibited the lowest concentrations of trace gases and the least pronounced average daily maximum concentrations in OH and HO_2^* concentrations, measured at $2.23 \pm 1.95 \times 10^6$ and $7.63 \pm 7.66 \times 10^7\,cm^{-3}$, respectively. This phase coincided with an increase in cloudy days and a decrease in temperatures, indicating reduced photochemical conditions.

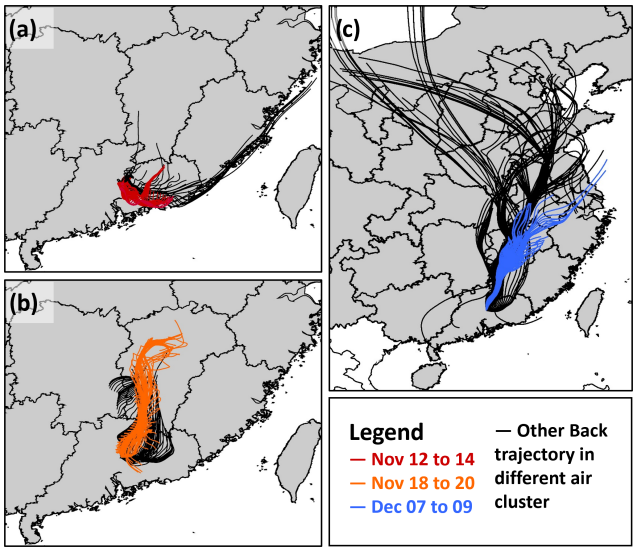

Figure 4. The 24 h back trajectories for the **(a)** Pearl River Delta (5 d), **(b)** central eastern China (4 d), and **(c)** central northern China (14 d) cases. The 3 d selected from each cluster for model simulation is distinguished by different colors.

3.1.2 Selection of cases

For each phase, a representative 3 d period was selected for detailed analysis based on the availability of comprehensive data and sunny conditions (colored trajectories in Fig. 4). In the subsequent analysis, PRD, CEC, and CNC refer to the selected periods corresponding to the air masses originating from these regions. The average daily maximum concentrations of OH and HO_2^* radicals for these periods are presented in Table 1. The average daily max OH concentrations were $6.89 \pm 1.10 \times 10^6$ cm^3 in PRD, $4.90 \pm 1.47 \times 10^6$ cm^3 in CEC, and $5.27 \pm 0.89 \times 10^6$ cm^3 in CNC, with a pronounced decrease from PRD to CEC (of 1.99×10^6 cm^3). The average daily max HO_2^* concentrations were $2.32 \pm 1.25 \times 10^8$ cm^3 in PRD, $2.36 \pm 0.92 \times 10^8$ cm^3 in CEC, and $1.82 \pm 1.02 \times 10^8$ cm^3 in CNC, with a slight increase of 0.04×10^8 cm^3 from PRD to CEC and a more substantial decrease of 0.54×10^8 cm^3 from CEC to CNC. These trends suggest a declining atmospheric oxidation capacity from PRD to CNC.

The precursor concentrations and meteorological parameters also varied across cases in terms of statistics (Tables 1 and S4) and diurnal variations (Fig. 5). In the PRD case, the average mixing ratios are characteristic of a rural environment, with AVOCs at 9.70 ± 5.00 ppb, OVOCs at 3.20 ± 2.30 ppb, isoprene at 0.26 ± 0.34 ppb, NO_2 at 6.3 ± 2.5 ppb, and NO at 0.73 ± 1.09 ppb. The NO concentration was affected by traffic sources, as there were no other fresh emission sources nearby, and the diurnal variation in NO showed a morning peak in all three cases (Fig. 5). In the CEC case, a general reduction in anthropogenic influence is evident. AVOCs, OVOCs, isoprene, and NO_2 drop significantly to 6.90 ± 1.80, 1.70 ± 0.38, 0.16 ± 0.20, and 4.84 ± 2.23 ppb, respectively. Meanwhile, NO levels remain close to PRD levels at 0.69 ± 1.00 ppb. In the CNC case, the air mass was more aged with reduced biogenic emissions, reflected in further decreases in isoprene and NO_2 to 0.03 ± 0.04 and 4.52 ± 1.97 ppb, respectively, due to colder weather conditions. The temperature decreased significantly from PRD to CNC, whereas the average peak photolysis frequency was comparable between PRD and CNC, as shown in Table 1.

3.2 Chemical budgets of OH and HO_2

To investigate the OH and HO_2 chemical budgets during the three distinct periods, we employed a box model constrained by observed concentrations of NO_x, VOCs, and relevant meteorological parameters in the selected cases (base scenario in which OH and HO_2 concentrations were not constrained by the measurements). The resulting OH and HO_2 budgets, displaying typical bell-shaped patterns, are illustrated in Fig. 6. During midday, the recycling of RO species becomes the dominant pathway for HO_2 production, with rates of 3.22 ppb h^{-1} for PRD, 2.09 ppb h^{-1} for CEC, and 1.08 ppb h^{-1} for CNC. Additionally, HCHO photolysis contributed 0.75, 0.46, and 0.26 ppb h^{-1} for PRD, CEC, and CNC, respectively. The sinks of HO_2 varied among the cases, with a minor contribution from the uptake process, driven by radical termination mechanisms. The rate of radical self-reactions decreased from PRD to CNC. In contrast, NO_x radical reactions between CEC and CNC were comparable, with respective rates of 0.39 and 0.33 ppb h^{-1}, indicating a shift in radical termination mechanisms.

OH formation was predominantly driven by the $HO_2 + NO$ reaction, contributing 5.18, 3.51, and 1.81 ppb h^{-1} (midday average for 10:00–15:00 UTC, referred to hereafter in this section) for PRD, CEC, and CNC, respectively. Additionally, contributions from ozone photolysis and HONO increased from PRD to CEC and then to CNC, with rates of 21.4 %, 22.7 %, and 24.6 %, respectively. The primary sinks for OH included reactions with VOCs to produce RO_2, with rates of 3.31, 2.02, and 1.13 ppb h^{-1}, and reactions with CO and other VOCs to generate HO_2, contributing 1.55, 1.06, and 0.38 ppb h^{-1} for PRD, CEC, and CNC, respectively. These findings highlight the critical role of OH + VOC reactions in the chemical budget of OH.

3.3 Comparison of model with observation results

Modeled OH and HO_2 concentrations were evaluated by comparing them against observations. The observed HO_2^* serves as an upper limit for ambient HO_2 due to the interference from RO_2. According to model simulations (Text S3), RO_2 interference was estimated to account for 56 %, 54 %,

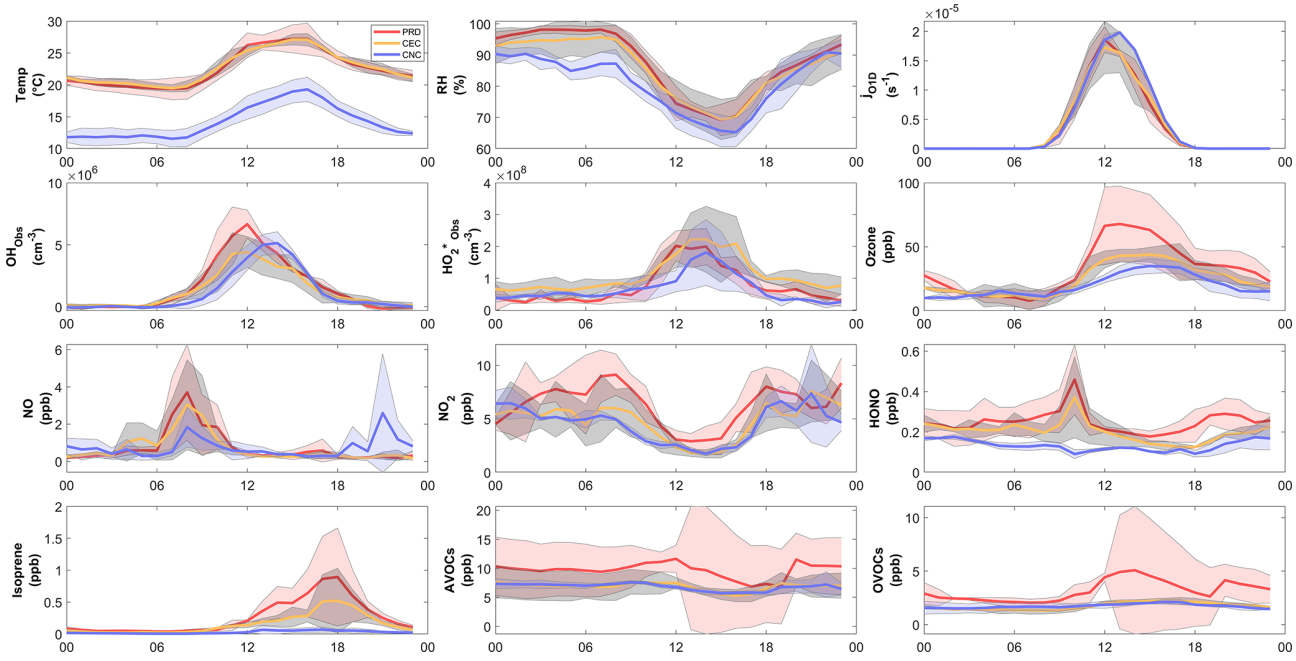

Figure 5. Average diurnal variations in **(a)** temperature, **(b)** relative humidity, **(c)** J_{O1D}, **(d)** OH, **(e)** HO_2^*, **(f)** ozone, **(g)** NO, **(h)** NO_2, **(i)** HONO, **(j)** isoprene, **(k)** AVOCs, and **(l)** OVOCs. The solid-colored lines represent the selected cases: orange for PRD, green for CEC, and blue for CNC. The light band represents the standard deviations of the mean. The increase in the standard deviations of VOCs and OVOCs during the PRD case is a result of an absence of data on the afternoon of 15 November and large variations on 12 and 13 November.

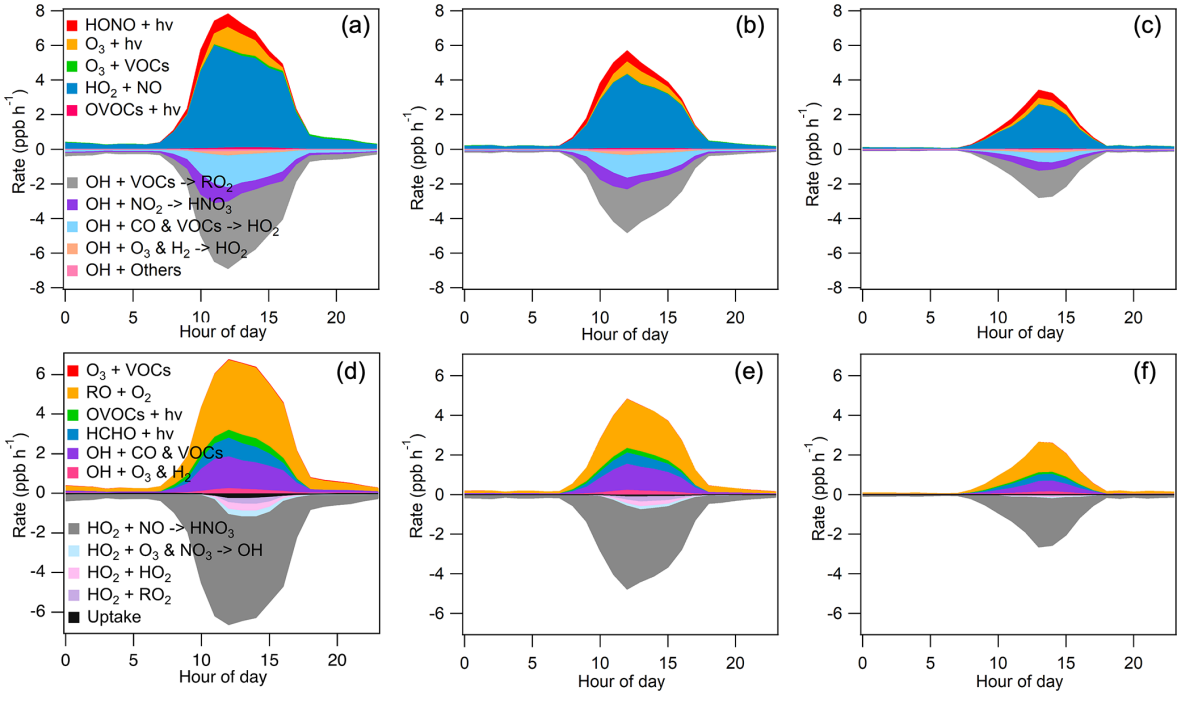

Figure 6. Chemical budgets of OH and HO_2 for PRD **(a, d)**, CEC **(b, e)**, and CNC **(c, f)** simulated using a chemical box model.

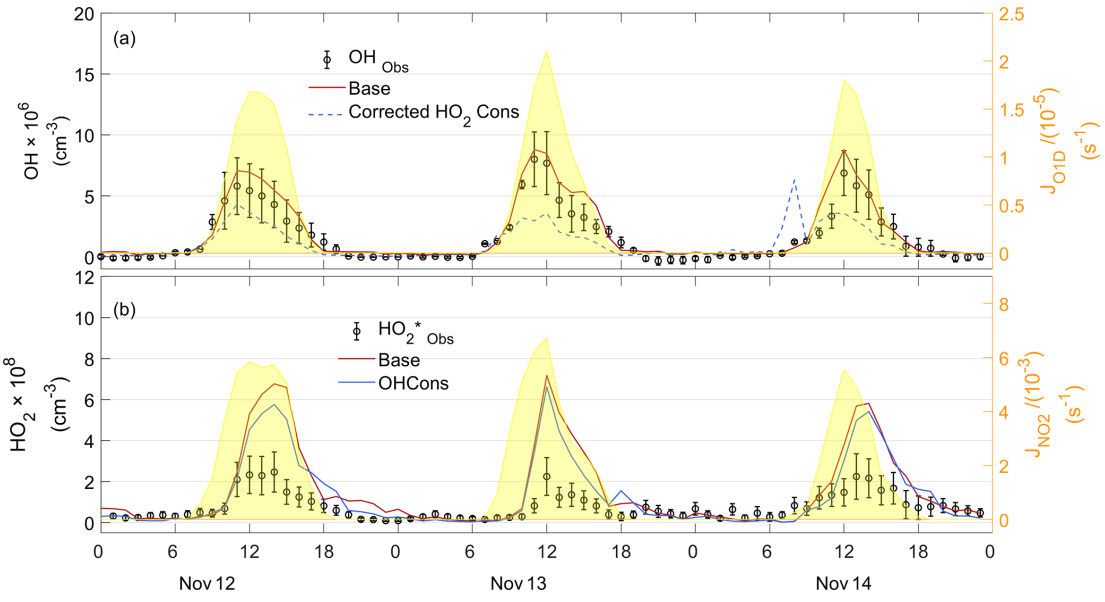

Figure 7. Observed and simulated OH, observed HO_2^*, and simulated HO_2 time series for the PRD case. The "Obs" subscript denotes the observation data. "Base" denotes the result of the baseline scenario, as described in Sect. 2.3. "Cons" denotes the results with additional constrained species compared to the baseline scenario.

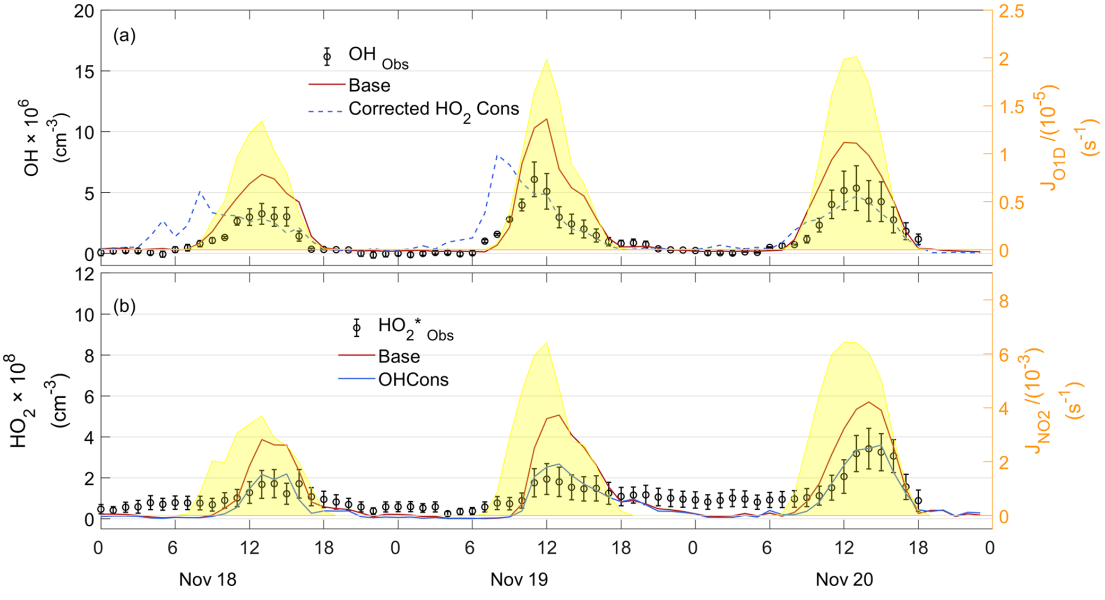

Figure 8. Observed and simulated OH, observed HO_2^*, and simulated HO_2 time series for the CEC case. The "Obs" subscript denotes the observation data. "Base" denotes the result of the baseline scenario, as described in Sect. 2.3. "Cons" denotes the results with additional constrained species compared to the baseline scenario.

and 59 % of the observed HO_2^* signal for the PRD, CEC, and CNC cases, respectively. In the PRD case (Fig. 7), which represents the most polluted and warmest environment among the three cases, the model slightly overestimated OH concentrations. However, the modeled HO_2 concentration was substantially higher than the observed HO_2^*, indicating an overprediction of HO_2. Similar overestimations have been reported at a rural site (Kanaya et al., 2012). For the CEC case (Fig. 8), the modeled OH and HO_2 concentrations were moderately higher than the observed values during the daytime, consistent with findings from a rural forest site (Bottorff et al., 2023). In the CNC case (Fig. 9), the model generally reproduced the observed OH trend, with HO_2 comparable to the observed HO_2^*. However, on 7 December, it exhib-

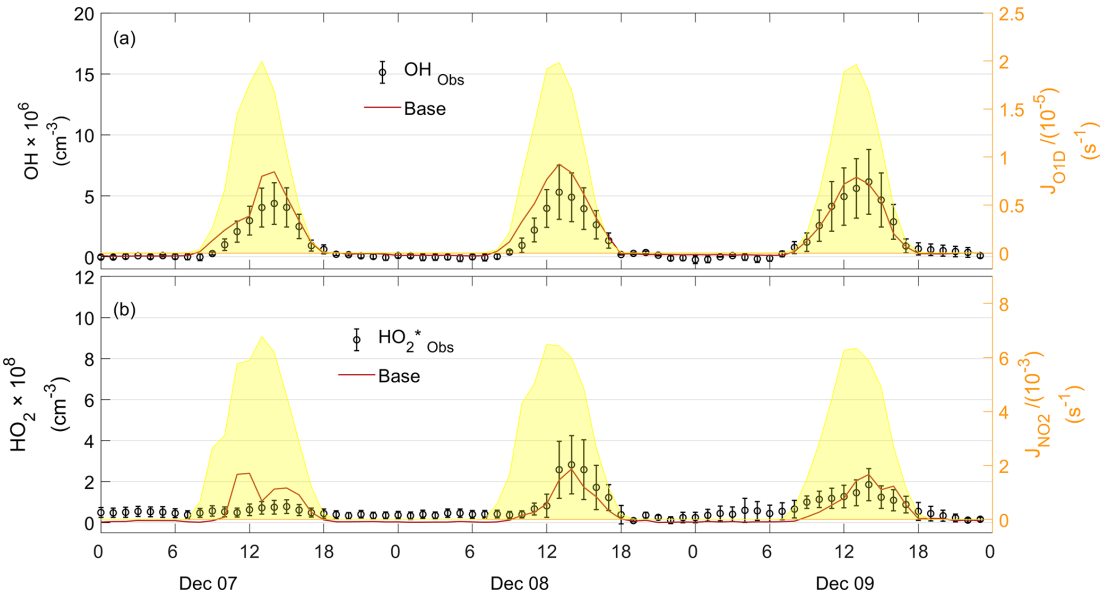

Figure 9. Observed and simulated time series of OH and HO_2^* for the CNC case. "Base" denotes the results of the baseline scenario, as described in Sect. 2.3.

ited daytime overestimation of HO_x, similar to the PRD case. At night, both CNC and CEC showed lower modeled HO_2 concentrations compared to observed HO_2^*, which can be explained by the expected contribution of RO_2 interference to HO_2^* in the observations. To further investigate the possible reasons for the model–observation discrepancies, sensitivity tests were conducted. The modeled RO_2 interference ratio was used to correct HO_2^* values, roughly estimating ambient HO_2 as input for the tests.

3.3.1 Substantial overestimation of HO_2 in PRD case

To explain the HO_2 overprediction by the base model, we constrained OH or corrected HO_2^* and compared these to the base case (without constraining OH and HO_2). Results show that constraining corrected HO_2^* (blue line in Fig. 7a) causes the model to underestimate OH, while constraining OH still leads to a substantially higher modeled HO_2 concentration (blue line in Fig. 7b) than the observed HO_2^*. This result suggests that to align the modeled OH and HO_2 with observations, it may be necessary to introduce a strong, unknown process for HO_2 that efficiently recycles OH with a high yield (Kanaya et al., 2012).

3.3.2 Moderate overestimation of both OH and HO_2 radicals in CEC case

Unlike the PRD case, constraining either OH or corrected HO_2^* in the CEC case generally reduces the daytime overestimation of both HO_2 and OH. These results indicate an additional sink for both OH and HO_2, as suggested by Bottorff et al. (2023). However, the OH concentration is overestimated in the morning when the corrected HO_2^* is constrained, suggesting that some OH sinks may be missing in the model during this period or that the corrected HO_2^* values that were used to constrain the model are still higher than the true HO_2 values. To further investigate the underlying causes, we examined the correlations between various pollutants. The significant negative correlation between CO and NO ($R^2 = 0.49$, $p = 0.01$, Fig. S6b) suggests that morning conditions in the CEC case may have been influenced by emission from fresh complete combustion during the CEC case, while correlations in the PRD and CNC cases are not significant (Fig. S6a and c). This indicates that the missing OH reactivity in the CEC case during the morning hours is possibly related to fresh vehicle emissions.

4 Implication for model overestimation of HO_x

OH and HO_2 are key species that determine the atmosphere's oxidative processes. Inaccurate modeling of their sinks can lead to significant overestimations of oxidation capacity, which may skew assessments of the impact of HO_x on air pollution and climate change. This problem is particularly pronounced in the case of ozone, a widespread photochemical pollutant. To demonstrate this issue, we compared results from two modeling scenarios: the first scenario was the base case (as described in Sect. 3.2), while the second scenario included constraints from all observational parameters, including measurements of OH and HO_2^*. Results for the scenario constrained by OH and corrected HO_2^* measurements are also shown in Figs. 10 and 11.

As illustrated in Fig. 10, not constraining free-radical measurement data in the chemical model (the orange lines) led

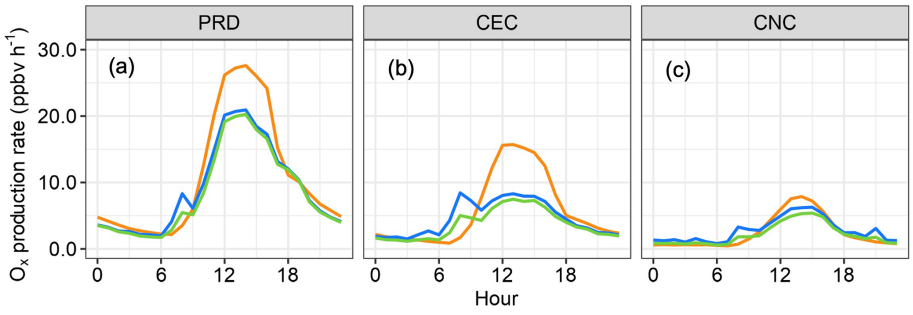

Figure 10. O_x ($O_3 + NO_2$) photochemical production rates in three comparative cases: **(a)** PRD, **(b)** CEC, and **(c)** CNC. The orange, green, and blue lines represent rates modeled by excluding OH and HO_2^*, including OH with corrected HO_2^*, and including OH with uncorrected HO_2^*, respectively.

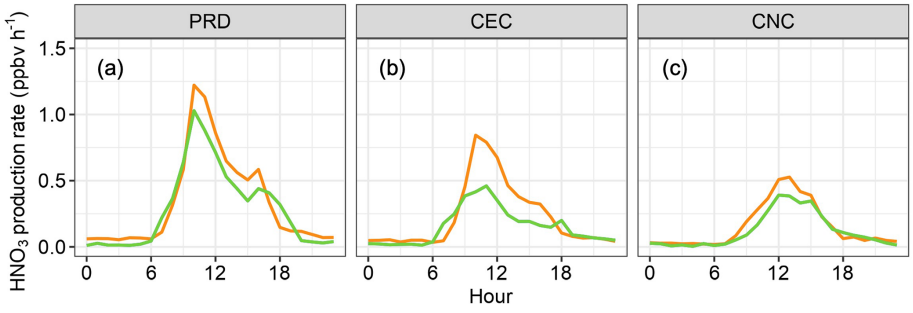

Figure 11. Modeled HNO_3 production rates in three comparative cases: **(a)** PRD, **(b)** CEC, and **(c)** CNC. The orange, green, and blue lines represent rates modeled by excluding OH and HO_2^*, including OH with corrected HO_2^*, and including OH with uncorrected HO_2^*, respectively. (The blue lines are covered by the green lines as the daytime HNO_3 production rates are determined by the constrained OH.)

to overestimates of ozone's photochemical production rates. Compared to scenarios constrained by OH and HO_2^*, in the PRD case, simulated midday O_x ($O_3 + NO_2$) formation rates in the base case were overestimated by 33 % on average and 32 % at peak O_x rates. In the CEC case, the overestimation was 79 % on average and 89 % at peak O_x rates, while in the CNC case, the smallest overestimation was 17 % on average and 25 % at peak. Since the ambient HO_2 concentration is lower than the constrained HO_2^* concentration, the impact of the overestimated HO_x on ozone production rates might be even larger in such environments (the green lines in Fig. 10).

The overestimation of HO_x also significantly affected the simulated concentration of nitric acid (HNO_3), which is crucial for new particle formation and growth (Wang et al., 2020). Figure 11 illustrates that the chemical model moderately overestimated nitric acid production rates without the constraints of free-radical measurements (the orange lines). Compared to the scenarios constrained by OH and HO_2^*, the midday production rates of nitric acid were overestimated by 25 %, 88 %, and 31 % in the PRD, CEC, and CNC cases, respectively. Such overestimations can considerably impact assessments of new particle formation and growth processes and their impact on air pollution and climate change. On the other hand, the impact on HNO_3 production is dominated by OH radicals; therefore, measurement interference of HO_2 is negligible.

5 Conclusion

HO_2^* and OH concentrations were measured using a chemical ionization mass spectrometer at a subtropical rural site in southern China from 12 November to 19 December 2022. The measurements indicated generally lower concentrations of OH and HO_2^* than those observed in previous studies at various sites. The model estimated that interferences from RO_2 contributed to 44 %–69 % of the HO_2^* throughout the campaign. Backward-trajectory analysis revealed three distinct phases characterized by sequentially decreasing pollution levels and temperatures. During the cold, clean period, model simulations closely matched the observed OH and HO_2^* concentrations. However, during the warm, polluted period, the models overestimated HO_2 or both radicals. Model sensitivity analysis indicates that adding an OH cycling reaction from HO_2 or additional sinks of OH and HO_2 would largely reduce the model–observation discrepancy in different cases of this study. However, the exact chemical reactions remain to be identified. Our results are in line with previous studies, indicating substantial gaps in our understanding of the sources and sinks of OH and HO_2 in certain en-

vironments. Our study provides additional evidence of the current incomplete understanding of HO_x sources and sinks and calls for more research to resolve the model–observation mismatch found in this work and in previous studies.

The overprediction of HO_x resulted in significant overestimation of the production rates of other secondary pollutants at the site, such as ozone and nitric acid. It is critical to evaluate the capability of OH and HO_2 simulations in major chemical transport models and Earth system models, as inaccurate simulations of OH and HO_2 may misguide the development of air pollution and global warming control strategies.

Data availability. All of the data used to produce this paper can be obtained by contacting Tao Wang (tao.wang@polyu.edu.hk).

Supplement. The supplement related to this article is available online at https://doi.org/10.5194/acp-25-8147-2025-supplement.

Author contributions. TW conceived the HO_x research. TW, XW, and YZ planned and organized the overall field campaign in Conghua. ZZ conducted the HO_x measurements using CIMS, with contributions from TW, WS, QC, and SH. XF, ZR, XL, AG, QW, CP, and XT performed the JNO_2 VOC and OVOC measurements. ZZ performed chemical box modeling with contributions from TC and QC. TC, ZZ, and TW analyzed the data and interpreted the results. ZZ analyzed the time series and diurnal variations in observation data, TC interpreted the results of the box model and investigated the missing sources, and TW supervised and guided these processes. TC, ZZ, and TW wrote the paper. All of the authors reviewed and commented on the paper.

Competing interests. At least one of the (co-)authors is a member of the editorial board of *Atmospheric Chemistry and Physics*. The peer-review process was guided by an independent editor, and the authors also have no other competing interests to declare.

Disclaimer. Publisher's note: Copernicus Publications remains neutral with regard to jurisdictional claims made in the text, published maps, institutional affiliations, or any other geographical representation in this paper. While Copernicus Publications makes every effort to include appropriate place names, the final responsibility lies with the authors.

Acknowledgements. We thank David Tanner, Wei Pu, Weihao Wang, and Zhe Wang for developing PolyU-CIMS. We are also grateful to the Guangzhou Institute of Geochemistry, Chinese Academy of Sciences, for providing access to its station and data on trace gases.

Financial support. This research was financially supported by the Hong Kong Research Grants Council (T24-504/17-N and 15223221 to Tao Wang), the National Science Foundation of China (42293322 to Tao Wang), and The Hong Kong Polytechnic University Postdoc Matching Fund Scheme (P0043403 to Tianshu Chen).

Review statement. This paper was edited by Kelvin Bates and reviewed by four anonymous referees.

References

Berresheim, H., Elste, T., Tremmel, H. G., Allen, A. G., Hansson, H.-C., Rosman, K., Dal Maso, M., Mäkelä, J. M., Kulmala, M., and O'Dowd, C. D.: Gas-aerosol relationships of H_2SO_4, MSA, and OH: Observations in the coastal marine boundary layer at Mace Head, Ireland, J. Geophys. Res.-Atmos., 107, PAR 5-1–PAR 5-12, https://doi.org/10.1029/2000JD000229, 2002.

Bottorff, B., Lew, M. M., Woo, Y., Rickly, P., Rollings, M. D., Deming, B., Anderson, D. C., Wood, E., Alwe, H. D., Millet, D. B., Weinheimer, A., Tyndall, G., Ortega, J., Dusanter, S., Leonardis, T., Flynn, J., Erickson, M., Alvarez, S., Rivera-Rios, J. C., Shutter, J. D., Keutsch, F., Helmig, D., Wang, W., Allen, H. M., Slade, J. H., Shepson, P. B., Bertman, S., and Stevens, P. S.: OH, HO_2, and RO_2 radical chemistry in a rural forest environment: measurements, model comparisons, and evidence of a missing radical sink, Atmos. Chem. Phys., 23, 10287–10311, https://doi.org/10.5194/acp-23-10287-2023, 2023.

Carslaw, N., Creasey, D. J., Heard, D. E., Lewis, A. C., McQuaid, J. B., Pilling, M. J., Monks, P. S., Bandy, B. J., and Penkett, S. A.: Modeling OH, HO_2, and RO_2 radicals in the marine boundary layer: 1. Model construction and comparison with field measurements, J. Geophys. Res., 104, 30241–30255, https://doi.org/10.1029/1999JD900783, 1999.

Chen, Q., Xia, M., Peng, X., Yu, C., Sun, P., Li, Y., Liu, Y., Xu, Z., Xu, Z., Wu, R., Nie, W., Ding, A., Zhao, Y., and Wang, T.: Large Daytime Molecular Chlorine Missing Source at a Suburban Site in East China, J. Geophys. Res.-Atmos., 127, e2021JD035796, https://doi.org/10.1029/2021JD035796, 2022.

Edwards, G. D., Cantrell, C. A., Stephens, S., Hill, B., Goyea, O., Shetter, R. E., Mauldin, R. L., Kosciuch, E., Tanner, D. J., and Eisele, F. L.: Chemical Ionization Mass Spectrometer Instrument for the Measurement of Tropospheric HO_2 and RO_2, Anal. Chem., 75, 5317–5327, https://doi.org/10.1021/ac034402b, 2003.

Eisele, F. L. and Tanner, D. J.: Ion-assisted tropospheric OH measurements, J. Geophys. Res., 96, 9295, https://doi.org/10.1029/91JD00198, 1991.

Eisele, F. L. and Tanner, D. J.: Measurement of the gas phase concentration of H_2SO_4 and methane sulfonic acid and estimates of H_2SO_4 production and loss in the atmosphere, J. Geophys. Res.-Atmos., 98, 9001–9010, https://doi.org/10.1029/93JD00031, 1993.

Feiner, P. A., Brune, W. H., Miller, D. O., Zhang, L., Cohen, R. C., Romer, P. S., Goldstein, A. H., Keutsch, F. N., Skog, K. M., Wennberg, P. O., Nguyen, T. B., Teng, A. P., DeGouw, J., Koss, A., Wild, R. J., Brown, S. S., Guenther, A., Edgerton, E., Baumann, K., and Fry, J. L.: Testing Atmospheric Ox-

idation in an Alabama Forest, J. Atmos. Sci., 73, 4699–4710, https://doi.org/10.1175/JAS-D-16-0044.1, 2016.

Fuchs, H., Bohn, B., Hofzumahaus, A., Holland, F., Lu, K. D., Nehr, S., Rohrer, F., and Wahner, A.: Detection of HO_2 by laser-induced fluorescence: calibration and interferences from RO_2 radicals, Atmos. Meas. Tech., 4, 1209–1225, https://doi.org/10.5194/amt-4-1209-2011, 2011.

Fuchs, H., Acir, I.-H., Bohn, B., Brauers, T., Dorn, H.-P., Häseler, R., Hofzumahaus, A., Holland, F., Kaminski, M., Li, X., Lu, K., Lutz, A., Nehr, S., Rohrer, F., Tillmann, R., Wegener, R., and Wahner, A.: OH regeneration from methacrolein oxidation investigated in the atmosphere simulation chamber SAPHIR, Atmos. Chem. Phys., 14, 7895–7908, https://doi.org/10.5194/acp-14-7895-2014, 2014.

Griffith, S. M., Hansen, R. F., Dusanter, S., Stevens, P. S., Alaghmand, M., Bertman, S. B., Carroll, M. A., Erickson, M., Galloway, M., Grossberg, N., Hottle, J., Hou, J., Jobson, B. T., Kammrath, A., Keutsch, F. N., Lefer, B. L., Mielke, L. H., O'Brien, A., Shepson, P. B., Thurlow, M., Wallace, W., Zhang, N., and Zhou, X. L.: OH and HO_2 radical chemistry during PROPHET 2008 and CABINEX 2009 – Part 1: Measurements and model comparison, Atmos. Chem. Phys., 13, 5403–5423, https://doi.org/10.5194/acp-13-5403-2013, 2013.

Guo, J., Wang, Z., Tao Wang, and Zhang, X.: Theoretical evaluation of different factors affecting the HO_2 uptake coefficient driven by aqueous-phase first-order loss reaction, Sci. Total Environ., 683, 146–153, https://doi.org/10.1016/j.scitotenv.2019.05.237, 2019.

Hanke, M., Uecker, J., Reiner, T., and Arnold, F.: Atmospheric peroxy radicals: ROXMAS, a new mass-spectrometric methodology for speciated measurements of HO_2 and σRO_2 and first results, Int. J. Mass Spectrom., 213, 91–99, https://doi.org/10.1016/S1387-3806(01)00548-6, 2002.

Hansen, R. F., Griffith, S. M., Dusanter, S., Rickly, P. S., Stevens, P. S., Bertman, S. B., Carroll, M. A., Erickson, M. H., Flynn, J. H., Grossberg, N., Jobson, B. T., Lefer, B. L., and Wallace, H. W.: Measurements of total hydroxyl radical reactivity during CABINEX 2009 – Part 1: field measurements, Atmos. Chem. Phys., 14, 2923–2937, https://doi.org/10.5194/acp-14-2923-2014, 2014.

Heard, D. E. and Pilling, M. J.: Measurement of OH and HO_2 in the Troposphere, Chem. Rev., 103, 5163–5198, https://doi.org/10.1021/cr020522s, 2003.

Hens, K., Novelli, A., Martinez, M., Auld, J., Axinte, R., Bohn, B., Fischer, H., Keronen, P., Kubistin, D., Nölscher, A. C., Oswald, R., Paasonen, P., Petäjä, T., Regelin, E., Sander, R., Sinha, V., Sipilä, M., Taraborrelli, D., Tatum Ernest, C., Williams, J., Lelieveld, J., and Harder, H.: Observation and modelling of HO_x radicals in a boreal forest, Atmos. Chem. Phys., 14, 8723–8747, https://doi.org/10.5194/acp-14-8723-2014, 2014.

Hofzumahaus, A., Rohrer, F., Lu, K., Bohn, B., Brauers, T., Chang, C.-C., Fuchs, H., Holland, F., Kita, K., Kondo, Y., Li, X., Lou, S., Shao, M., Zeng, L., Wahner, A., and Zhang, Y.: Amplified Trace Gas Removal in the Troposphere, Science, 324, 1702–1704, https://doi.org/10.1126/science.1164566, 2009.

Jacob, D.: Heterogeneous chemistry and tropospheric ozone, Atmos. Environ., 34, 2131–2159, https://doi.org/10.1016/S1352-2310(99)00462-8, 2000.

Jeong, D., Seco, R., Emmons, L., Schwantes, R., Liu, Y., McKinney, K. A., Martin, S. T., Keutsch, F. N., Gu, D., Guenther, A. B., Vega, O., Tota, J., Souza, R. A. F., Springston, S. R., Watson, T. B., and Kim, S.: Reconciling Observed and Predicted Tropical Rainforest OH Concentrations, J. Geophys. Res.-Atmos., 127, e2020JD032901, https://doi.org/10.1029/2020JD032901, 2022.

Kanaya, Y., Cao, R., Kato, S., Miyakawa, Y., Kajii, Y., Tanimoto, H., Yokouchi, Y., Mochida, M., Kawamura, K., and Akimoto, H.: Chemistry of OH and HO_2 radicals observed at Rishiri Island, Japan, in September 2003: Missing daytime sink of HO_2 and positive nighttime correlations with monoterpenes, J. Geophys. Res., 112, D11308, https://doi.org/10.1029/2006JD007987, 2007.

Kanaya, Y., Hofzumahaus, A., Dorn, H.-P., Brauers, T., Fuchs, H., Holland, F., Rohrer, F., Bohn, B., Tillmann, R., Wegener, R., Wahner, A., Kajii, Y., Miyamoto, K., Nishida, S., Watanabe, K., Yoshino, A., Kubistin, D., Martinez, M., Rudolf, M., Harder, H., Berresheim, H., Elste, T., Plass-Dülmer, C., Stange, G., Kleffmann, J., Elshorbany, Y., and Schurath, U.: Comparisons of observed and modeled OH and HO_2 concentrations during the ambient measurement period of the HO_xComp field campaign, Atmos. Chem. Phys., 12, 2567–2585, https://doi.org/10.5194/acp-12-2567-2012, 2012.

Kim, S., Wolfe, G. M., Mauldin, L., Cantrell, C., Guenther, A., Karl, T., Turnipseed, A., Greenberg, J., Hall, S. R., Ullmann, K., Apel, E., Hornbrook, R., Kajii, Y., Nakashima, Y., Keutsch, F. N., DiGangi, J. P., Henry, S. B., Kaser, L., Schnitzhofer, R., Graus, M., Hansel, A., Zheng, W., and Flocke, F. F.: Evaluation of HO_x sources and cycling using measurement-constrained model calculations in a 2-methyl-3-butene-2-ol (MBO) and monoterpene (MT) dominated ecosystem, Atmos. Chem. Phys., 13, 2031–2044, https://doi.org/10.5194/acp-13-2031-2013, 2013.

Kürten, A., Rondo, L., Ehrhart, S., and Curtius, J.: Calibration of a Chemical Ionization Mass Spectrometer for the Measurement of Gaseous Sulfuric Acid, J. Phys. Chem. A, 116, 6375–6386, https://doi.org/10.1021/jp212123n, 2012.

Lelieveld, J., Butler, T. M., Crowley, J. N., Dillon, T. J., Fischer, H., Ganzeveld, L., Harder, H., Lawrence, M. G., Martinez, M., Taraborrelli, D., and Williams, J.: Atmospheric oxidation capacity sustained by a tropical forest, Nature, 452, 737–740, https://doi.org/10.1038/nature06870, 2008.

Lew, M. M., Rickly, P. S., Bottorff, B. P., Reidy, E., Sklaveniti, S., Léonardis, T., Locoge, N., Dusanter, S., Kundu, S., Wood, E., and Stevens, P. S.: OH and HO_2 radical chemistry in a midlatitude forest: measurements and model comparisons, Atmos. Chem. Phys., 20, 9209–9230, https://doi.org/10.5194/acp-20-9209-2020, 2020.

Lou, S., Holland, F., Rohrer, F., Lu, K., Bohn, B., Brauers, T., Chang, C. C., Fuchs, H., Häseler, R., Kita, K., Kondo, Y., Li, X., Shao, M., Zeng, L., Wahner, A., Zhang, Y., Wang, W., and Hofzumahaus, A.: Atmospheric OH reactivities in the Pearl River Delta – China in summer 2006: measurement and model results, Atmos. Chem. Phys., 10, 11243–11260, https://doi.org/10.5194/acp-10-11243-2010, 2010.

Ma, X., Tan, Z., Lu, K., Yang, X., Liu, Y., Li, S., Li, X., Chen, S., Novelli, A., Cho, C., Zeng, L., Wahner, A., and Zhang, Y.: Winter photochemistry in Beijing: Observation and model simulation of OH and HO_2 radicals at an urban site, Sci. Total Environ., 685, 85–95, https://doi.org/10.1016/j.scitotenv.2019.05.329, 2019.

Ma, X., Tan, Z., Lu, K., Yang, X., Chen, X., Wang, H., Chen, S., Fang, X., Li, S., Li, X., Liu, J., Liu, Y., Lou, S., Qiu, W., Wang,

H., Zeng, L., and Zhang, Y.: OH and HO_2 radical chemistry at a suburban site during the EXPLORE-YRD campaign in 2018, Atmos. Chem. Phys., 22, 7005–7028, https://doi.org/10.5194/acp-22-7005-2022, 2022.

Mallik, C., Tomsche, L., Bourtsoukidis, E., Crowley, J. N., Derstroff, B., Fischer, H., Hafermann, S., Hüser, I., Javed, U., Keßel, S., Lelieveld, J., Martinez, M., Meusel, H., Novelli, A., Phillips, G. J., Pozzer, A., Reiffs, A., Sander, R., Taraborrelli, D., Sauvage, C., Schuladen, J., Su, H., Williams, J., and Harder, H.: Oxidation processes in the eastern Mediterranean atmosphere: evidence from the modelling of HO_x measurements over Cyprus, Atmos. Chem. Phys., 18, 10825–10847, https://doi.org/10.5194/acp-18-10825-2018, 2018.

Mao, J., Ren, X., Zhang, L., Van Duin, D. M., Cohen, R. C., Park, J.-H., Goldstein, A. H., Paulot, F., Beaver, M. R., Crounse, J. D., Wennberg, P. O., DiGangi, J. P., Henry, S. B., Keutsch, F. N., Park, C., Schade, G. W., Wolfe, G. M., Thornton, J. A., and Brune, W. H.: Insights into hydroxyl measurements and atmospheric oxidation in a California forest, Atmos. Chem. Phys., 12, 8009–8020, https://doi.org/10.5194/acp-12-8009-2012, 2012.

Mauldin III, R. L., Kosciuch, E., Henry, B., Eisele, F. L., Shetter, R., Lefer, B., Chen, G., Davis, D., Huey, G., and Tanner, D.: Measurements of OH, $HO_2 + RO_2$, H_2SO_4, and MSA at the South Pole during ISCAT 2000, Atmos. Environ., 38, 5423–5437, https://doi.org/10.1016/j.atmosenv.2004.06.031, 2004.

Muller, J. B. A., Elste, T., Plass-Dülmer, C., Stange, G., Holla, R., Claude, A., Englert, J., Gilge, S., and Kubistin, D.: A novel semi-direct method to measure OH reactivity by chemical ionization mass spectrometry (CIMS), Atmos. Meas. Tech., 11, 4413–4433, https://doi.org/10.5194/amt-11-4413-2018, 2018.

Novelli, A., Hens, K., Tatum Ernest, C., Kubistin, D., Regelin, E., Elste, T., Plass-Dülmer, C., Martinez, M., Lelieveld, J., and Harder, H.: Characterisation of an inlet pre-injector laser-induced fluorescence instrument for the measurement of atmospheric hydroxyl radicals, Atmos. Meas. Tech., 7, 3413–3430, https://doi.org/10.5194/amt-7-3413-2014, 2014.

Novelli, A., Vereecken, L., Bohn, B., Dorn, H.-P., Gkatzelis, G. I., Hofzumahaus, A., Holland, F., Reimer, D., Rohrer, F., Rosanka, S., Taraborrelli, D., Tillmann, R., Wegener, R., Yu, Z., Kiendler-Scharr, A., Wahner, A., and Fuchs, H.: Importance of isomerization reactions for OH radical regeneration from the photooxidation of isoprene investigated in the atmospheric simulation chamber SAPHIR, Atmos. Chem. Phys., 20, 3333–3355, https://doi.org/10.5194/acp-20-3333-2020, 2020.

Sjostedt, S. J., Huey, L. G., Tanner, D. J., Peischl, J., Chen, G., Dibb, J. E., Lefer, B., Hutterli, M. A., Beyersdorf, A. J., Blake, N. J., Blake, D. R., Sueper, D., Ryerson, T., Burkhart, J., and Stohl, A.: Observations of hydroxyl and the sum of peroxy radicals at Summit, Greenland during summer 2003, Atmos. Environ., 41, 5122–5137, https://doi.org/10.1016/j.atmosenv.2006.06.065, 2007.

Slater, E. J., Whalley, L. K., Woodward-Massey, R., Ye, C., Lee, J. D., Squires, F., Hopkins, J. R., Dunmore, R. E., Shaw, M., Hamilton, J. F., Lewis, A. C., Crilley, L. R., Kramer, L., Bloss, W., Vu, T., Sun, Y., Xu, W., Yue, S., Ren, L., Acton, W. J. F., Hewitt, C. N., Wang, X., Fu, P., and Heard, D. E.: Elevated levels of OH observed in haze events during wintertime in central Beijing, Atmos. Chem. Phys., 20, 14847–14871, https://doi.org/10.5194/acp-20-14847-2020, 2020.

Stone, D., Whalley, L. K., and Heard, D. E.: Tropospheric OH and HO_2 radicals: field measurements and model comparisons, Chem. Soc. Rev., 41, 6348, https://doi.org/10.1039/c2cs35140d, 2012.

Tan, D., Faloona, I., Simpas, J. B., Brune, W., Shepson, P. B., Couch, T. L., Sumner, A. L., Carroll, M. A., Thornberry, T., Apel, E., Riemer, D., and Stockwell, W.: HO_x budgets in a deciduous forest: Results from the PROPHET summer 1998 campaign, J. Geophys. Res., 106, 24407–24427, https://doi.org/10.1029/2001JD900016, 2001.

Tan, Z., Fuchs, H., Lu, K., Hofzumahaus, A., Bohn, B., Broch, S., Dong, H., Gomm, S., Häseler, R., He, L., Holland, F., Li, X., Liu, Y., Lu, S., Rohrer, F., Shao, M., Wang, B., Wang, M., Wu, Y., Zeng, L., Zhang, Y., Wahner, A., and Zhang, Y.: Radical chemistry at a rural site (Wangdu) in the North China Plain: observation and model calculations of OH, HO_2 and RO_2 radicals, Atmos. Chem. Phys., 17, 663–690, https://doi.org/10.5194/acp-17-663-2017, 2017.

Tan, Z., Rohrer, F., Lu, K., Ma, X., Bohn, B., Broch, S., Dong, H., Fuchs, H., Gkatzelis, G. I., Hofzumahaus, A., Holland, F., Li, X., Liu, Y., Liu, Y., Novelli, A., Shao, M., Wang, H., Wu, Y., Zeng, L., Hu, M., Kiendler-Scharr, A., Wahner, A., and Zhang, Y.: Wintertime photochemistry in Beijing: observations of RO_x radical concentrations in the North China Plain during the BEST-ONE campaign, Atmos. Chem. Phys., 18, 12391–12411, https://doi.org/10.5194/acp-18-12391-2018, 2018.

Tan, Z., Lu, K., Hofzumahaus, A., Fuchs, H., Bohn, B., Holland, F., Liu, Y., Rohrer, F., Shao, M., Sun, K., Wu, Y., Zeng, L., Zhang, Y., Zou, Q., Kiendler-Scharr, A., Wahner, A., and Zhang, Y.: Experimental budgets of OH, HO_2, and RO_2 radicals and implications for ozone formation in the Pearl River Delta in China 2014, Atmos. Chem. Phys., 19, 7129–7150, https://doi.org/10.5194/acp-19-7129-2019, 2019.

Tanner, D. J. and Eisele, F. L.: Present OH measurement limits and associated uncertainties, J. Geophys. Res., 100, 2883, https://doi.org/10.1029/94JD02609, 1995.

Tanner, D. J., Jefferson, A., and Eisele, F. L.: Selected ion chemical ionization mass spectrometric measurement of OH, J. Geophys. Res., 102, 6415–6425, https://doi.org/10.1029/96JD03919, 1997.

Thames, A. B., Brune, W. H., Miller, D. O., Allen, H. M., Apel, E. C., Blake, D. R., Bui, T. P., Commane, R., Crounse, J. D., Daube, B. C., Diskin, G. S., DiGangi, J. P., Elkins, J. W., Hall, S. R., Hanisco, T. F., Hannun, R. A., Hintsa, E., Hornbrook, R. S., Kim, M. J., McKain, K., Moore, F. L., Nicely, J. M., Peischl, J., Ryerson, T. B., St. Clair, J. M., Sweeney, C., Teng, A., Thompson, C. R., Ullmann, K., Wennberg, P. O., and Wolfe, G. M.: Missing OH reactivity in the global marine boundary layer, Atmos. Chem. Phys., 20, 4013–4029, https://doi.org/10.5194/acp-20-4013-2020, 2020.

Wang, M., Kong, W., Marten, R., He, X.-C., Chen, D., Pfeifer, J., Heitto, A., Kontkanen, J., Dada, L., Kürten, A., Yli-Juuti, T., Manninen, H. E., Amanatidis, S., Amorim, A., Baalbaki, R., Baccarini, A., Bell, D. M., Bertozzi, B., Bräkling, S., Brilke, S., Murillo, L. C., Chiu, R., Chu, B., De Menezes, L.-P., Duplissy, J., Finkenzeller, H., Carracedo, L. G., Granzin, M., Guida, R., Hansel, A., Hofbauer, V., Krechmer, J., Lehtipalo, K., Lamkaddam, H., Lampimäki, M., Lee, C. P., Makhmutov, V., Marie, G., Mathot, S., Mauldin, R. L., Mentler, B., Müller, T., Onnela, A.,

Partoll, E., Petäjä, T., Philippov, M., Pospisilova, V., Ranjithkumar, A., Rissanen, M., Rörup, B., Scholz, W., Shen, J., Simon, M., Sipilä, M., Steiner, G., Stolzenburg, D., Tham, Y. J., Tomé, A., Wagner, A. C., Wang, D. S., Wang, Y., Weber, S. K., Winkler, P. M., Wlasits, P. J., Wu, Y., Xiao, M., Ye, Q., Zauner-Wieczorek, M., Zhou, X., Volkamer, R., Riipinen, I., Dommen, J., Curtius, J., Baltensperger, U., Kulmala, M., Worsnop, D. R., Kirkby, J., Seinfeld, J. H., El-Haddad, I., Flagan, R. C., and Donahue, N. M.: Rapid growth of new atmospheric particles by nitric acid and ammonia condensation, Nature, 581, 184–189, https://doi.org/10.1038/s41586-020-2270-4, 2020.

Wang, X., Jacob, D. J., Eastham, S. D., Sulprizio, M. P., Zhu, L., Chen, Q., Alexander, B., Sherwen, T., Evans, M. J., Lee, B. H., Haskins, J. D., Lopez-Hilfiker, F. D., Thornton, J. A., Huey, G. L., and Liao, H.: The role of chlorine in global tropospheric chemistry, Atmos. Chem. Phys., 19, 3981–4003, https://doi.org/10.5194/acp-19-3981-2019, 2019.

Wennberg, P. O., Bates, K. H., Crounse, J. D., Dodson, L. G., McVay, R. C., Mertens, L. A., Nguyen, T. B., Praske, E., Schwantes, R. H., Smarte, M. D., St Clair, J. M., Teng, A. P., Zhang, X., and Seinfeld, J. H.: Gas-Phase Reactions of Isoprene and Its Major Oxidation Products, Chem. Rev., 118, 3337–3390, https://doi.org/10.1021/acs.chemrev.7b00439, 2018.

Whalley, L. K., Furneaux, K. L., Goddard, A., Lee, J. D., Mahajan, A., Oetjen, H., Read, K. A., Kaaden, N., Carpenter, L. J., Lewis, A. C., Plane, J. M. C., Saltzman, E. S., Wiedensohler, A., and Heard, D. E.: The chemistry of OH and HO_2 radicals in the boundary layer over the tropical Atlantic Ocean, Atmos. Chem. Phys., 10, 1555–1576, https://doi.org/10.5194/acp-10-1555-2010, 2010.

Whalley, L. K., Edwards, P. M., Furneaux, K. L., Goddard, A., Ingham, T., Evans, M. J., Stone, D., Hopkins, J. R., Jones, C. E., Karunaharan, A., Lee, J. D., Lewis, A. C., Monks, P. S., Moller, S. J., and Heard, D. E.: Quantifying the magnitude of a missing hydroxyl radical source in a tropical rainforest, Atmos. Chem. Phys., 11, 7223–7233, https://doi.org/10.5194/acp-11-7223-2011, 2011.

Whalley, L. K., Blitz, M. A., Desservettaz, M., Seakins, P. W., and Heard, D. E.: Reporting the sensitivity of laser-induced fluorescence instruments used for HO_2 detection to an interference from RO_2 radicals and introducing a novel approach that enables HO_2 and certain RO_2 types to be selectively measured, Atmos. Meas. Tech., 6, 3425–3440, https://doi.org/10.5194/amt-6-3425-2013, 2013.

Wolfe, G. M., Marvin, M. R., Roberts, S. J., Travis, K. R., and Liao, J.: The Framework for 0-D Atmospheric Modeling (F0AM) v3.1, Geosci. Model Dev., 9, 3309–3319, https://doi.org/10.5194/gmd-9-3309-2016, 2016.

Woodward-Massey, R., Slater, E. J., Alen, J., Ingham, T., Cryer, D. R., Stimpson, L. M., Ye, C., Seakins, P. W., Whalley, L. K., and Heard, D. E.: Implementation of a chemical background method for atmospheric OH measurements by laser-induced fluorescence: characterisation and observations from the UK and China, Atmos. Meas. Tech., 13, 3119–3146, https://doi.org/10.5194/amt-13-3119-2020, 2020.

Xu, Z., Xue, L., Wang, T., Xia, T., Gao, Y., Louie, P. K. K., and Luk, C. W. Y.: Measurements of Peroxyacetyl Nitrate at a Background Site in the Pearl River Delta Region: Production Efficiency and Regional Transport, Aerosol Air Qual. Res., 15, 833–841, https://doi.org/10.4209/aaqr.2014.11.0275, 2015.

Yang, X., Lu, K., Ma, X., Liu, Y., Wang, H., Hu, R., Li, X., Lou, S., Chen, S., Dong, H., Wang, F., Wang, Y., Zhang, G., Li, S., Yang, S., Yang, Y., Kuang, C., Tan, Z., Chen, X., Qiu, P., Zeng, L., Xie, P., and Zhang, Y.: Observations and modeling of OH and HO_2 radicals in Chengdu, China in summer 2019, Sci. Total Environ., 772, 144829, https://doi.org/10.1016/j.scitotenv.2020.144829, 2021.

Yang, X., Lu, K., Ma, X., Gao, Y., Tan, Z., Wang, H., Chen, X., Li, X., Huang, X., He, L., Tang, M., Zhu, B., Chen, S., Dong, H., Zeng, L., and Zhang, Y.: Radical chemistry in the Pearl River Delta: observations and modeling of OH and HO_2 radicals in Shenzhen in 2018, Atmos. Chem. Phys., 22, 12525–12542, https://doi.org/10.5194/acp-22-12525-2022, 2022.

Yang, Y., Shao, M., Wang, X., Nölscher, A. C., Kessel, S., Guenther, A., and Williams, J.: Towards a quantitative understanding of total OH reactivity: A review, Atmos. Environ., 134, 147–161, https://doi.org/10.1016/j.atmosenv.2016.03.010, 2016.

Zou, Z., Chen, Q., Xia, M., Yuan, Q., Chen, Y., Wang, Y., Xiong, E., Wang, Z., and Wang, T.: OH measurements in the coastal atmosphere of South China: possible missing OH sinks in aged air masses, Atmos. Chem. Phys., 23, 7057–7074, https://doi.org/10.5194/acp-23-7057-2023, 2023.